Novel Thermoplastic Fibre-Metal Laminates Manufactured by Vacuum Resin Infusion: The Effect of Surface Treatments on Interfacial Bonding

Materials and Design 162 (2019) 331–344

Contents lists available at ScienceDirect

Materials and Design

journal homepage: www.elsevier.com/locate/matdes

Novel thermoplastic fibre-metal laminates manufactured by vacuum resin infusion: The effect of surface treatments on interfacial bonding

Dimitrios Mamalis, Winifred Obande, Vasileios Koutsos, Jane R. Blackford, Conchúr M. Ó Brádaigh, Dipa Ray *

School of Engineering, Institute for Materials and Processes, The University of Edinburgh, King's Buildings, Edinburgh EH9 3FB, United Kingdom

HIGHLIGHTS

- Resin-infused thermoplastic fibre-metal laminates (TP-FML) have been manufactured.
- Surface treatments on the aluminium alloy enhanced the bond strength between metal and composite.
- TP-FML has been mechanically assessed and compared to an equivalent thermoplastic composite.
- Improvements on interfacial bond strength have been investigated by mode-I fracture toughness testing.

GRAPHICAL ABSTRACT

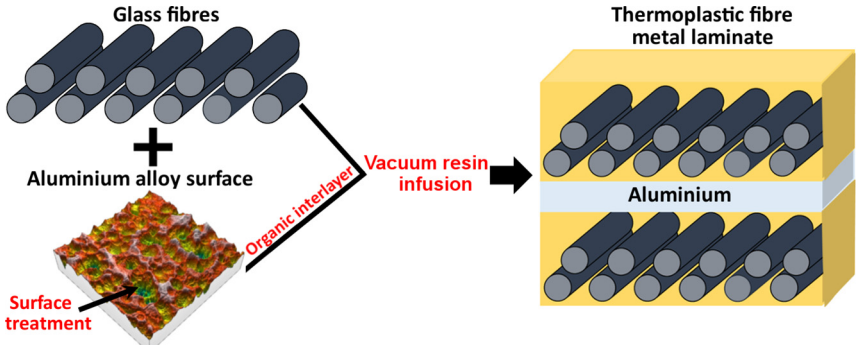

ARTICLE INFO

Article history:
Received 26 October 2018
Received in revised form 21 November 2018
Accepted 22 November 2018
Available online 26 November 2018

Keywords:
Fibre-metal laminates
Thermoplastic matrix
Surface treatments
Interface bonding
Mechanical properties

ABSTRACT

The manufacturing process of a new generation of thermoplastic fibre-metal laminates (TP-FMLs) was investigated. A vacuum assisted resin infusion method was used to produce the hybrid laminates. The effect of various chemical and physical treatments on the surface morphology of the aluminium (Al) alloy sheets and on the bond strength at the metal-composite interface was examined. The wettability, topography and chemical composition of the treated Al alloy sheets were studied by employing contact-angle goniometry, coherence scanning interferometry, profilometry and X-ray photoelectron spectroscopy. The results showed that the applied treatments on the Al alloy sheet changed the surface morphology and surface energy in a different degree, which in turn effectively enhanced the interfacial bond strength between the constituents. In addition, the flexural, interlaminar shear strength and interlaminar fracture toughness of the manufactured TP-FMLs with the optimum metal surface treatment were evaluated. The experimental results of the TP-FMLs were compared to an equivalent thermoplastic composite. The composite-metal interface and the fracture surface characteristics were examined under scanning electron microscopy. In-situ polymerisation was found to play a key role in bonding the treated Al alloy with the composite layer during manufacturing.

1. Introduction

Fibre-metal laminates (FMLs) are hybrids comprising of preferentially stacked layers of thin metal sheets and fibre-reinforced polymers (FRPs). They offer a combination of the favourable characteristics of monolithic metallic alloys and FRPs, making them ideal candidates for weight-critical applications with requirements for fatigue and impact resistance [1,2]. Other advantages of FMLs include high corrosion resistance, low environmental degradation and enhanced fire resistance [3].

First generation FMLs such as those comprising of glass fibre reinforcement, epoxy matrix systems and aluminium — i.e., the GLARE™

* Corresponding author.
E-mail address: Dipa.Roy@ed.ac.uk (D. Ray).

https://doi.org/10.1016/j.matdes.2018.11.048

Table 1
Chemical composition of the aluminium alloy (as supplied from the respective manufacturer [28]).

Material	Al	Si	Fe	Cu	Mn	Mg	Cr	Ni	Zn	Ti	Pb	Others
Al 6082-T6 (wt%)	98	0.9	0.38	0.07	0.49	0.02	0.01	0.06	0.03	0.01	0.01	0.03

family, and their aramid-reinforced counterparts in the ARALL™ family, have been used extensively in the aerospace sector [3]. However, manufacturing of these thermoset-based FMLs are associated with long process cycle times, and they cannot be recycled or reshaped. Furthermore, thermosets are brittle and typically have low fracture toughness [4,5].

In an effort to address the issues with long processing cycles, the vacuum-assisted resin transfer moulding (VaRTM) technique was utilised in the fabrication of second-generation FMLs. The use of this process is concomitantly cost-effective due to the replacement of high cost pre-impregnated materials with lower cost dry fabric reinforcements [1]; facilitating the adoption of FMLs into non-aerospace sectors. Considering the aforementioned drawbacks in the reprocessibility and repairability of thermosetting FMLs, in this study, thermoplastic (TP)-based FMLs were developed. TP matrices such as polyetherimide, polyetheretherketone, polypropylene and polyimide have been investigated by researchers [4–9]. These FMLs offer several benefits, which include thermoformability, weldability, recyclability and improved toughness compared to their thermosetting counterparts [10–14]. However, an obvious limitation of such matrix systems is their high melt viscosity, which necessitates high-temperature processing. Additionally, due to the non-reactive nature of the thermoplastics, adhesives have been used in the fabrication of these thermoplastic FMLs (TP-FMLs) to bond the FRP layer to the metal [3]. Advancing technology has resulted in the development of novel reactive TP resin systems, which are formulated for low-cost processing by resin permeation techniques such as VaRTM. The recently launched family of in-situ polymerisable thermoplastic acrylic resins — Elium® has received significant attention for FRP fabrication [15–19]. In combination with appropriate metal surface treatments and suitably selected organic coatings to enhance the fibre-metal interfacial bond strength, the low viscosity and in-situ polymerisation mechanism of Elium® could be exploited for the fabrication of new-generation TP-FMLs by a conventional resin infusion technique. Subsequent processing operations such as press forming and disassembly could be performed with relative ease.

Given their heterogeneous make-up, selection of the individual constituent material influences the performance of the FMLs. The ultimate performance of the FMLs, however, is not only determined by these individual constituents alone; their interfacial bond strength (i.e. the structural integrity of the interface between the metallic sheets and reinforced polymer layers) plays a significant role in the FML's performance [5]. While a lot of work has been published on metal surface treatment techniques and coatings to enhance composite adhesion with metals, most studies to-date have focused on the use of an etching or activation treatment and the subsequent application of a coating or adhesive to promote adhesion between the organic matrices to the inorganic metal substrate [20–27]. Therefore, surface treatments on the metal surface (e.g. steel or aluminium) prior to manufacturing is the most critical step in bonding the individual constituents, which cannot be disregarded in producing FMLs.

This paper aims to investigate the effects of varying chemical, electrochemical and physical treatments (plasma exposure) on the bond strength between the FRP and the metallic layers. Al alloy was used as the metallic constituent and Elium® resin/glass fibre (GF-Elium®) was used as the composite layer. The surface roughness and wettability of the treated Al alloy was examined by using scanning interferometry and contact-angle goniometry, respectively. The chemical compositions of the Al alloy samples before and after different surface treatments were investigated by employing X-ray photoelectron spectroscopy (XPS). An optimised metal surface treatment and coating technique was developed to achieve an acceptable level of composite/metal interfacial bonding. In-situ polymerisation played the key role in bonding the Al with the composite layer during FML manufacturing by VaRTM technique. Mechanical characterisation of the FMLs in terms of flexural and interlaminar shear strength was performed in comparison to an equivalent GF-Elium®. Moreover, the Mode-I interlaminar fracture toughness of the FMLs was also studied to assess the interfacial bond strength.

2. Experimental procedure

2.1. Materials

In the present investigation Elium® liquid thermoplastic resin, unidirectional glass reinforcement and Aluminium (Al) alloy 6082-T6 in the form of 0.71 mm thick sheet, were used to fabricate thermoplastic fibre-metal laminates (TP-FMLs). The Elium® 180 resin with viscosity and density of 100 mPa·s and 1.01 g/cm^3, respectively, was supplied by ARKEMA (France). An organic peroxide powder (BP-50-FT) was used as the initiator, supplied by United Initiators GmbH & Co. KG. The chemical composition of the used Al alloy 6082-T6 can be seen in Table 1, as provided from Wilsons Ltd. [28]. Unidirectional (UD) E-glass fabric (646 g/m^2) was the reinforcement supplied from Ahlstrom-Munksjö. More specifically, the fabric consisted of 600 g/m^2 E-glass fibres in 0° and 36 g/m^2 in 90° direction. The polymeric sizing on the surface of the E-glass fibres was multicompatible with polyester, vinyl ester and epoxy resins, as provided by Ahlstrom-Munksjö.

2.2. Surface treatments

Prior to surface treatments, the Al alloy sheets were acetone-wiped with lint-free tissues to degrease the surface and afterwards they were subjected to four different surface treatments, as displayed in Table 2. For the alkaline etching case, sodium hydroxide (NaOH) pellets were used for the preparation of the alkaline solution, which was supplied by Sigma-Aldrich, Inc. (Merck KGaA, Darmstadt, Germany). For the acid treatment, an acid etchant ANPE 80/5/5/10 used to etch the Al alloy sheets, supplied by MicroChemicals GmbH (Germany). The

Table 2
The different surface treatments applied to the Al alloys sheets

Time (min)	Treatment					
	NaOH 10 wt%	Acid solution (ANPE 80/5/5/10)	NaOH 10 wt% + acid solution	Acid solution + NaOH 10 wt%	Sulphuric acid anodising	Atmospheric plasma treatment
2	–	✓	–	–	Def Stan 2003–25/4	1 scan at 1 mm/s
5	✓	✓	✓	✓		1 scan at 2 mm/s
10	✓	✓	✓	✓		3 scans at 1 mm/s
20	✓	✓	✓	✓		3 scans at 2 mm/s

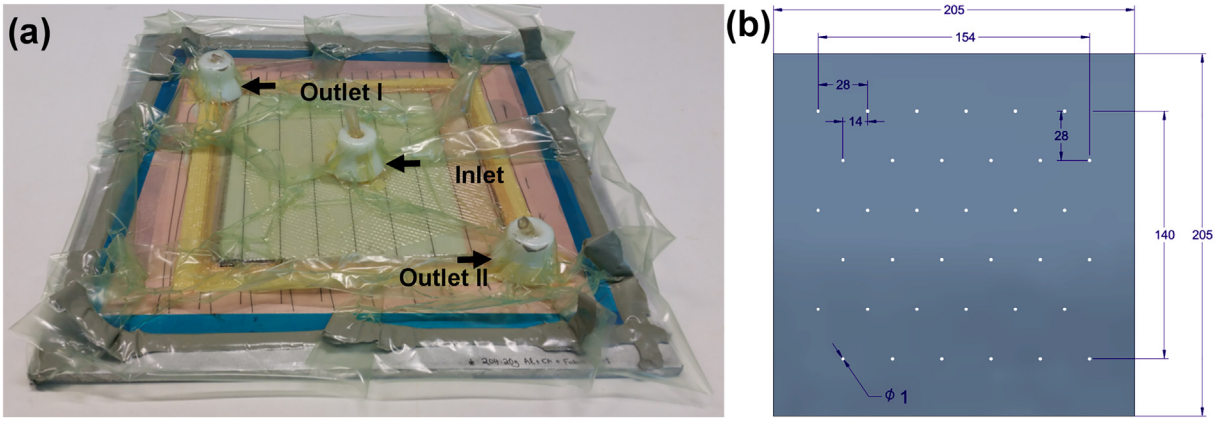

Fig. 1. (a) Representative image of the (radial) VaRTM process. (b) Hole-map design of the Al alloy sheet.

chemical composition of the etchant solution was the following: H_3PO_4:HNO_3:CH_3COOH:H_2O = 73%:3.1%:3.3%:20.6%. Note that the Al alloy sheets were immersed in NaOH and in acid etchant baths using a Pyrex container. Furthermore, Al alloy samples were electrochemically etched using anodising technique in a sulphuric acid (H_2SO_4) bath, provided by NPI-SOLUTIONS (United Kingdom). The Al alloy sheets were anodised by immersing them in the acid solution (the electrolyte) and applying DC (direct current) electricity in accordance with Def Stan 2003-25/4 [29]. Additionally, atmospheric plasma treatment of the Al alloy was carried out using a Cirrus, single nozzle unit, supplied by Henniker Plasma (United Kingdom). The system was operated at a pressure of 6 bar with the gas (compressed air) passed through a nozzle. The power was fixed at 300 W (nominal) and a radio frequency (RF) power at 40 kHz. A 0.5 mm source-to-substrate distance was set while number of scans (1 and 3) and scan speeds (1, 2, 5 and 10 mm/s) were altered. Table 2 shows the different chemical and physical (plasma) surface treatments applied on the Al alloy sheets.

2.3. Surface characterisation

2.3.1. Contact-angle goniometry

The wettability and surface free energy of the treated Al alloy samples were measured by means of the sessile drop technique using a DSA-10MK2 goniometer (KRUSS, Germany). Contact-angles of distilled water, at temperature and humidity of 20 ± 2 °C and 30 ± 5%, respectively, were measured using the Drop Shape Analysis (DSA) software. The purity of the distilled water was confirmed by correlation of the measured surface tension with the literature values for pure water (~72.8 mN/m at ~20 °C). In this regard, drops of distilled water (volumes of 2–3 μL) were deposited on the surface of the treated Al alloy samples and the contact-angle readings, which were the equilibrium contact-angle values, were measured and repeated more than twelve times across the surface of each sample. Note that the average contact-angle values for each applied treatment on the Al alloy samples were reported.

2.3.2. Surface topography

A Zygo NewView™ 8300 coherence scanning interferometer (CSI) was used to characterize the treated surfaces of the Al alloy samples. Coherence scanning interferometry offers three-dimensional (3D) measurement of surface topography with high precision and accuracy. Two different objective lenses, with magnifications of 20× and 50×, and field of view (X ∗ Y) 418 × 418 μm^2 and 167 × 167 μm^2, respectively, were used. Then a Gaussian 50-μm filter was applied to all the measurements to generate both roughness and waviness topography profiles. The analysis of 3D areal surface texture was conducted according to ISO 25178 (2012): Geometric Product Specifications (GPS). In particular, the standard defines 3D surface texture parameters and the associated specification operators. The statistical distribution parameter *Sa*, which represents the arithmetical mean height of the surfaces along the z axis, was measured. Note that over three Al alloy samples were examined for each case at each magnification.

Table 3
Measurements of contact-angle (CA), surface free energy γ_{SV} and work of adhesion (W_A) for the different surface treatments (±standard deviation). Note that the surface roughness measurements *Ra* and *Sa* were acquired from a SURFTEST SJ-410 profilometer and a Zygo NewView™ 8300 coherence scanning interferometer, respectively.

Al alloy treatment	CA (°)	γ_{SV} (mJ/m^2)	W_A (mJ)	*Ra* (μm)	*Sa* (μm) 50×
Degreased-only (acetone)	82 ± 1	34.3	82.9	0.376 ± 0.031	0.270 ± 0.028
5 min alkaline (10 wt%)	38 ± 1	60.4	130.1	0.467 ± 0.014	0.338 ± 0.016
10 min alkaline (10 wt%)	47 ± 1	55.5	122.4	0.595 ± 0.009	0.641 ± 0.021
20 min alkaline (10 wt%)	65 ± 2	44.8	103.6	0.825 ± 0.025	0.784 ± 0.035
2 min acid	38 ± 2.5	60.4	130.1	0.310 ± 0.022	0.215 ± 0.020
5 min acid	37 ± 3	61.0	130.9	0.308 ± 0.016	0.209 ± 0.028
10 min acid	55 ± 3	50.8	114.5	0.326 ± 0.014	0.220 ± 0.018
20 min acid	59 ± 3	48.4	110.3	0.334 ± 0.019	0.224 ± 0.022
20 min [alkaline (10 wt%) + acid]	61 ± 3.5	47.2	108.1	0.710 ± 0.021	0.682 ± 0.031
20 min [acid + alkaline (10 wt%)]	51 ± 3	53.2	118.6	0.572 ± 0.026	0.481 ± 0.027
Sulphuric acid anodising	57 ± 1	49.6	112.4	0.331 ± 0.015	0.263 ± 0.020
Plasma 1 scan at 1 mm/s	32 ± 2.5	63.5	134.5	0.301 ± 0.018	0.256 ± 0.015
Plasma 1 scan at 2 mm/s	35 ± 2.5	62.0	132.4	0.274 ± 0.014	0.212 ± 0.025
Plasma 1 scan at 5 mm/s	47 ± 2	55.5	130.1	0.321 ± 0.025	0.311 ± 0.019
Plasma 1 scan at 10 mm/s	63 ± 3.5	46.6	106.9	0.348 ± 0.031	0.326 ± 0.020
Plasma 3 scan at 1 mm/s	59 ± 5	48.4	110.3	0.292 ± 0.017	0.223 ± 0.021
Plasma 3 scan at 2 mm/s	50 ± 6	53.8	119.6	0.312 ± 0.019	0.247 ± 0.025

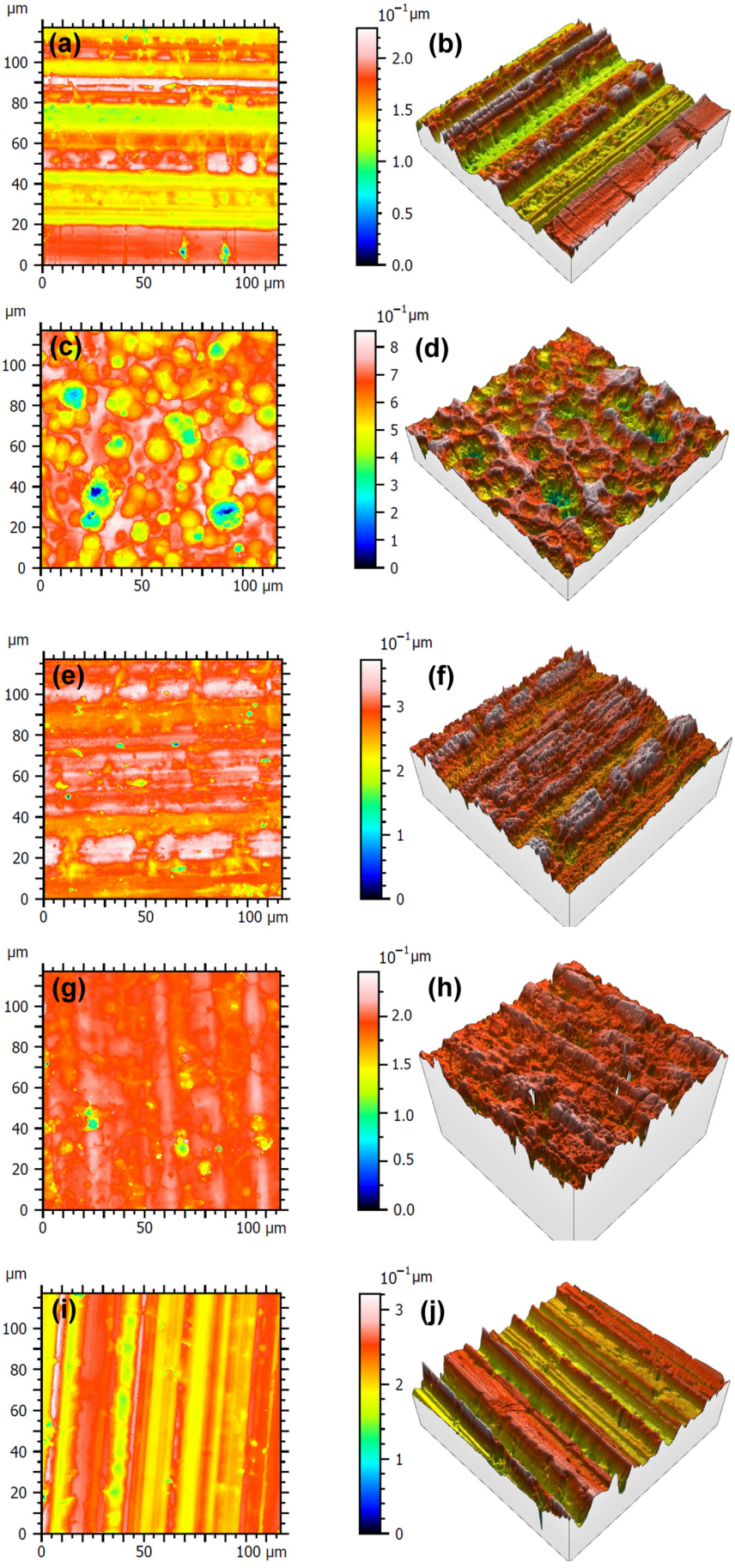
(a)
(b)
(c)
(d)
(e)
(f)
(g)
(h)
(i)
(j)
μm
10^{-1} μm
0
50
100 μm

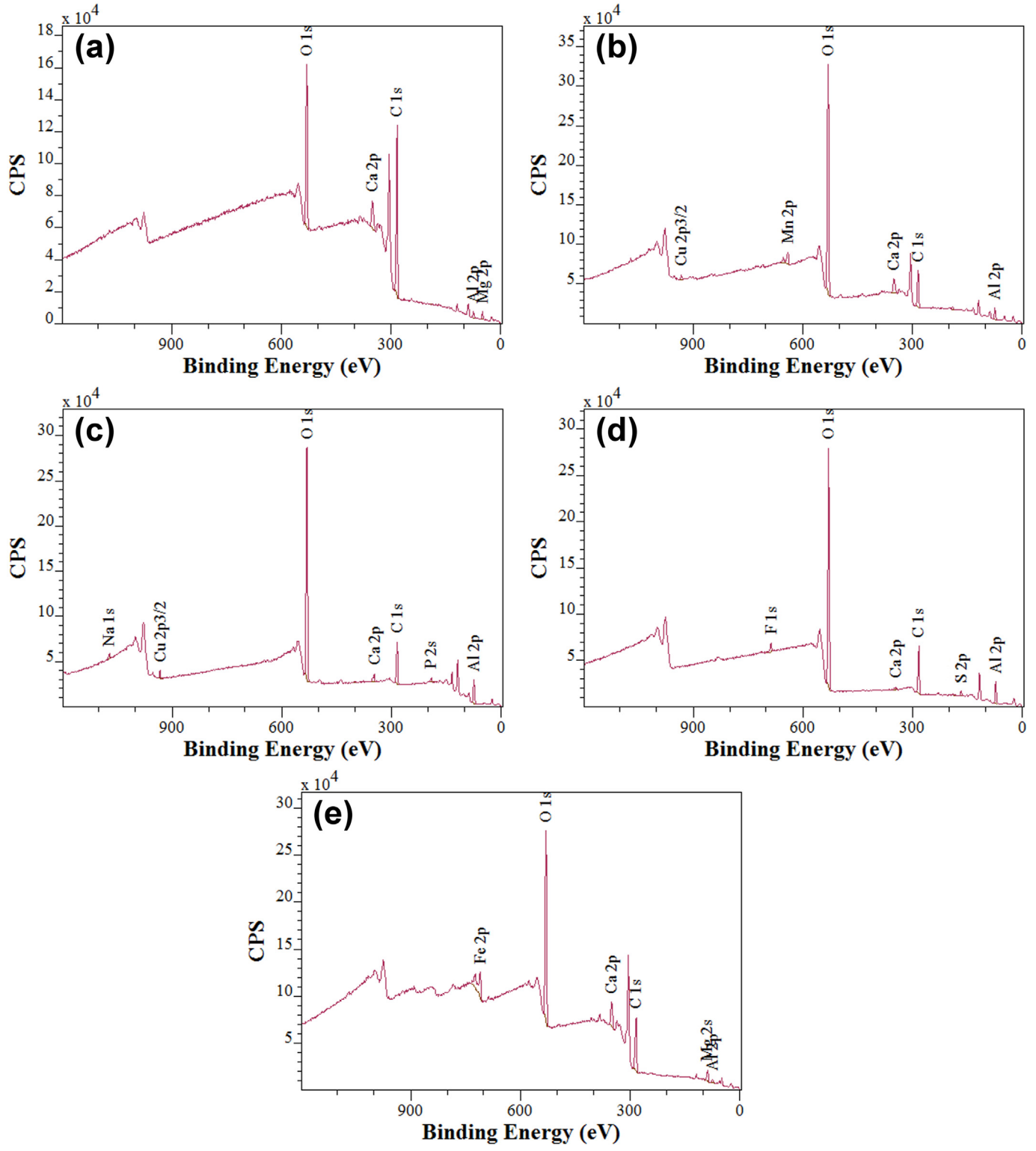

Fig. 3. XPS wide-scan spectrum of the Al alloy (6082-T6) samples after (a) degreasing-only, (b) alkaline (NaOH) (10 wt%) etching for 20 min, (c) acid etching for 20 min, (d) anodising and (e) atmospheric plasma treatment, 1 scan at 1 mm/s.

Additionally, macroscopic characterisation of the Al alloy samples was also performed using a mechanical stylus profilometer, SURFTEST SJ-410 series (Mitutoyo Corporation, Japan) and the roughness values *Ra* of the samples were evaluated in accordance with ISO 1997. *Ra* is the arithmetical average value of the departure of the profile above and below the mean line throughout the specified sampling length.

Fig. 2. Surface topography images of the (a) and (b) degreased-only Al alloy samples, (c) and (d) after alkaline etching for 20 min, (e) and (f) after acid treatment for 20 min, (g) and (h) after anodising and (i) and (j) after plasma exposure. Note that images (a), (c), (e), (g) and (i) show the 2D height profiles while micrographs (b), (d), (f), (h) and (j) depict 3D height profiles of the Al alloy samples.

The sampling length of surface selected in this evaluation was 13 mm and with a scan distance of 0.1 mm/s. Three scans were performed for each Al alloy sample.

All measurements were performed under controlled laboratory conditions at temperature of 20 ± 1 °C and relative humidity of 35 ± 10%, isolated from noise and dust.

2.3.3. X-ray photoelectron spectroscopy (XPS)

X-ray photoelectron spectroscopy was employed to characterize the surface chemical compositions and chemical states in the depth of nanometres before and after various surface treatments. XPS is recognised as an Ultra High Vacuum (UHV) technique, which is suitable for the quantitative determination of elemental composition (atomic %) in the surface region of the samples. This technique involves irradiating the surface of interest with soft X-rays and analysing the energy of the emitted photoelectrons. In this study, a Kratos Axis Ultra DLD system was used to collect XPS spectra using monochromatic Al *Kα* X-ray source operating at 120 W (10 mA × 12 kV). Data was collected with pass energies of 160 eV for survey spectra, and 40 eV for the high-resolution scans with step sizes of 1.0 eV and 0.1 eV respectively. The system was operated in the Hybrid mode, using a combination of magnetic immersion and electrostatic lenses and acquired over an area approximately 300 × 700 μm^2. A magnetically confined charge compensation system was used to minimize charging of the sample surface, and all spectra were taken with a 90° take-off angle. A base pressure of around 1×10^{-9} Torr was maintained during collection of the spectra. Data was analysed using CasaXPS (v2.3.19rev1.1) software after subtraction of a Shirley background and applying modified Wagner sensitivity factors, as supplied by the manufacturer.

2.4. Fabrication of TP-FMLs

All TP-FMLs were fabricated using a standard Vacuum-assisted Resin Transfer Moulding (VaRTM) technique. Fig. 1(a) depicts a typical image of the VaRTM set-up. Holes were drilled in the central zone of the Al alloy sheets in order to produce flow paths for the resin to permeate through the metal layer. The holes were drilled using a Computer Numerical Control (CNC) machine based on Ortiz de Mendibil et al. [1] as shown in Fig. 1(b). High dimensional precision and low roughness of the hole-map were obtained with the use of a CNC machine.

The stacking sequence of the manufactured TP-FML laminates was [0°$_3$/Al/0°$_3$] resulting in a 'sandwich' configuration where the core material was the Al alloy sheet. The thickness of the manufactured TP-FML plates was 3.5 ± 0.2 mm and the dimensions were ~210 × 210 mm^2. An epoxy acrylate coating (CN104), supplied by SARTOMER ARKEMA GROUP, was applied on the surface of the treated Al alloy sheets in order to enhance bonding between the composite and the Al alloy. Elium®-matrix laminates reinforced with UD E-glass fabric (GF-Elium®) were manufactured following the same processing cycle as described for the TP-FMLs to provide a baseline for comparison. The lay-up of the GF-Elium® laminates consisted of 8 layers [0$_6$] of E-glass fabric with a thickness of 3.6 ± 0.2 mm. Fibre volume fraction (FVF) and void content of all the processed laminates were determined by the burn-off technique according to ASTM D3171 (2009). The FVF and void content calculations of all the manufactured laminates were estimated to be ~49% and ~1.1%, respectively.

2.5. Mechanical testing

2.5.1. Flexural testing

The flexural properties of the manufactured TP-FMLs and GF-Elium® were investigated on a universal testing machine (Zwick/Roell, model Z010) using a three-point bending fixture at a crosshead speed of 1 mm/min, according to ASTM D7264 (2015). The specimen thickness was around 3.5 ± 0.3 mm following a span-to-thickness ratio of 32:1. The standard specimen width was 13 mm and the specimen length was about 20% longer than the support span. The radius of all the loading noses was 2 mm. Video extensometry (UVX — Imetrium systems) was used to record the deflection of the loaded samples. The flexure strength and modulus were determined by loading five or more specimens to failure for each test case. The stress was calculated for any point on the load–deflection curve by the following equation:

$$\sigma_f = 3PL/2bh^2 \tag{1}$$

where σ_f (MPa) is stress at the outer surface in the load span region, P (N) is the applied force, L (mm) is the support span length, b (mm) and h (mm) are the width and the thickness of tested specimen, respectively. In addition, the flexural modulus elasticity for the three-point bending method was expressed as:

$$E_f = L^3m/4bh^3 \tag{2}$$

where E_f (MPa) is the flexural modulus of elasticity, L, b, and h are the same as for Eq. (1), and m is the slope of the linear region of the load–displacement curve (N/m).

2.5.2. Interlaminar shear strength (ILSS)

The interlaminar shear strength of the TP-FMLs and the GF-Elium® composites was determined by a short beam shear test in accordance with EN ISO 14130 (1997). The load cell capacity of the measuring system was 50 kN (Zwick/Roell, model Z010). The thickness (h) of the tested samples was 3.5 ± 0.2 mm, the length (l) was 34 mm and the width (b) was 17 mm (following the ratios: $l = 10h$ and $b = 5h$, respectively). The radius of the loading member was 5 ± 0.2 mm and that of the two supports was 2 ± 0.2 mm. The apparent maximum interlaminar shear stress, τ_M, based on the beam theory was calculated as follows:

$$\tau_M = 3/4 \times F_M/bh \tag{3}$$

where F is the failure or maximum load (N), b is the width (mm) and h is the thickness of the test specimen.

2.5.3. Interlaminar fracture toughness test

In order to evaluate the interlaminar properties of the composites, Mode-I (G_{IC}) interlaminar fracture toughness tests were performed following ASTM D5528-13. The Mode-I tests were carried out at a crosshead displacement of 1 mm/min, at least five specimens for each type composite were tested. A 13-μm thick PTFE film of length 63 mm was inserted in the mid-plane of the laminate; between the Al alloy sheet and the composite. The film provided an initial crack with nominal delamination length of $a \approx 63$ mm. The manufactured laminates were carefully machined to extract the test specimens with dimension of 150 mm length, 25 mm width and nominal thickness ~3.5 ± 0.2 mm. Prior to testing, a white marker was applied at the edges of the specimens and then black dotes were painted in order to visualize the crack growth during testing. Tensile loading was applied through two loading blocks adhered to the end of each specimen and video

Table 4
Elemental surface composition of the Al alloy samples after the different chemical and physical (atmospheric plasma) treatments, determined by XPS (in at.%).

Treatment	Elements		
	C 1s	O 1s	Al 2p
Degreased-only	72.04	22.99	4.49
Alkaline (10 wt%) for 20 min	32.27	53.45	13.56
Acid for 20 min	26.15	41.93	18.49
Anodisation (Def Stan 03-25/4)	29.45	50.93	18.20
Atmospheric plasma (1 scan at 1 mm/s)	48.27	47.23	4.15

extensometry (UVX — Imetrium systems) was used to record the crack initiation and propagation for each test. The camera incorporated into the system is a Manta G-146B/G-146C and it is able to video-log at 17.8 frames per second. The Mode-I interlaminar fracture toughness, G_{IC}, was calculated using the modified beam theory (MBT), taking into account the rotation at the delamination front, as follows in Eq. (4):

$$G_{IC} = 3P\delta/2b(a + |\Delta|) \quad (4)$$

where P is the load, δ is the displacement, *b* is the specimen width, *a* is

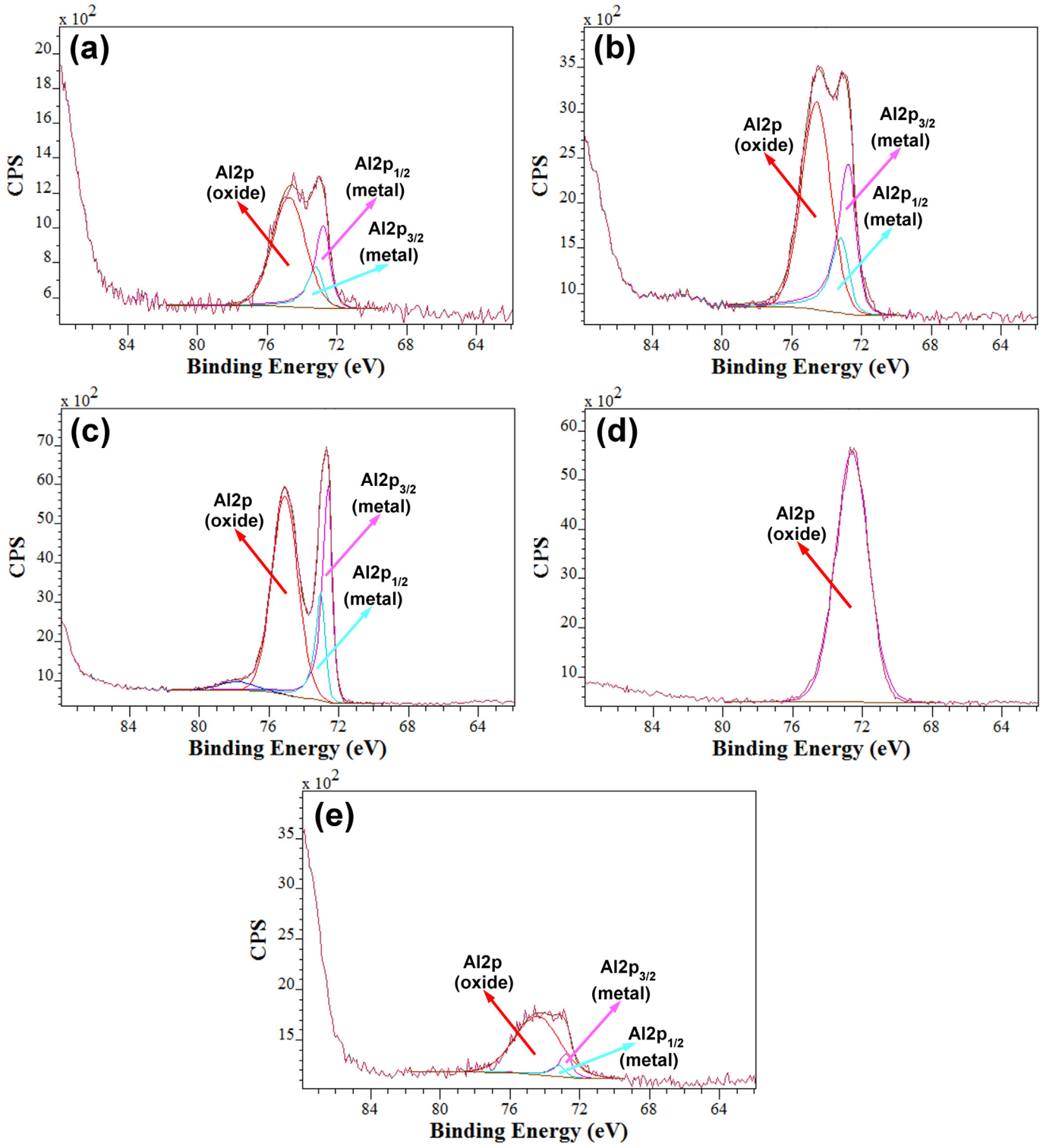

Fig. 4. Typical view of the Al 2p peaks measured at high-resolution XPS spectra of the treated Al alloys i.e. (a) degreased-only, (b) alkali-treated for 20 min, (c) acid-treated for 20 min, (d) anodised and (e) atmospheric plasma; 1 scan at 1 mm/s.

the delamination length, and Δ is the horizontal axis intercept from the linear a–$C^{1/3}$ curve. The compliance, C, is the ratio of displacement to corresponding load, δ/P. The initial value G_{IC} was obtained as the average of G_{IC} values at the ~50 mm delamination length.

2.6. Scanning electron microscopy (SEM)

The fracture surfaces of the TP-FMLs and GF-Elium® were examined with Hitachi SU-70 and Carl Zeiss SIGMA HD VP field emission scanning electron microscopes (FE-SEM). Prior to examination, the fracture surfaces were sputter-coated with a thin evaporated layer of gold for a period of 5–8 min reaching a thickness of approximately 100 Å.

3. Results and discussion

3.1. Surface wettability

Surface treatment of the Al alloy sheets is an important step prior to fabrication of TP-FMLs, in order to achieve an appropriate surface morphology and a stable oxide layer, which are necessary for improving the composite/metal bonding. Table 3 gives quantitative data of the treated Al alloy surfaces using various treatment techniques, where the contact-angle (CA), work of adhesion (W_A) and surface roughness values are listed. More specifically, the surface roughness parameters *Ra* and *Sa* (Table 3) were measured using a SURFTEST SJ-410 profilometer and a Zygo NewView™ 8300 coherence scanning interferometer, respectively. In addition, Fig. 2 shows typical 2D (left column) and 3D (right column) topography images for the treated Al alloy surfaces.

Contact-angle measurements were performed to evaluate the changes on the wettability of the Al alloy surfaces induced by the different surface treatments using the sessile drop method. The reported contact-angle values in Table 3 refer to measurements taken at four (major) directions of the Al alloy surface including 0°, 90° and ±45°. Note that a minimum of three drops were deposited in each direction and the final values represent averages of all measurements for each treatment case. The wettability of the Al alloy surface was studied by calculating the work of adhesion (W_A) and surface free energy (γ_{SV}) values according to the Young–Dupré equation [30] (Eq. (5)) and the Neumann [31] (Eq. (6)) equations, respectively.

$$W_A = \gamma_{LV}\,(1 + \cos\theta) \tag{5}$$

$$W_A = 2(\gamma_{LV}\cdot\gamma_{SV})^{1/2}\ \exp\left[-\beta(\gamma_{LV}-\gamma_{SV})^2\right] \tag{6}$$

where γ_{LV} and γ_{SV} are the surface tension of water ($\gamma_{LV} = 72.8$ mN/m^2) and surface free energy of the solid phase (Al alloy), respectively. θ is the water contact-angle and β is a constant with a value of 0.0001247 ± 0.000010 (mJ/m^2)$^{-2}$. To calculate the surface free energy of solid-vapour, the work of adhesion was first calculated from Eq. (5) and γ_{SV} was then calculated using Eq. (6). The results obtained for the probe liquid, i.e. distilled water, are presented in Table 3. Distilled water contact-angle and surface free energy values of 82° and 34.3 mJ/m^2, respectively, were measured on the degreased-only Al alloy case. The latter was indicative of low hydrophilicity of the degreased-only Al alloy sample due to the presence of the alumina oxide layer as well as hydrocarbons on its surface, which is expected to cause poor wettability. The poor wettability of the substrate is most likely to act as an inhibiting parameter in order to achieve a good adhesion strength between the Al alloy and the composite. The degreased-only Al surface was serrated as shown in the topography images in Fig. 2(a) and (b). It can be seen that the contact-angles were significantly reduced after the alkali and acid treatments, with short exposure times such as 5 min (Table 3). Consequently, the work of adhesion, the surface free energy and roughness were remarkably increased after the chemical etching due to removal of the oxide layer [20]. However, the wetting behaviour of the probe liquid was lowered, with longer exposure times such as 20 min. The chemical attack was more aggressive with longer treatment times for both alkali and acid resulting in rougher surfaces with decreased surface energy and work of adhesion (Table 3). Typical height profile images of the alkali and acid treated Al alloy surfaces, for an etching period of 20 min, are presented in Fig. 2(c)–(f). The alkaline etching created a microscopically rougher surface morphology (and removed surface contaminants [21]) which was characterised by larger number of craters on the Al alloy surface (see Fig. 2(c) and (d)). Furthermore, intermediate surface characteristics in terms of wettability and surface roughness were revealed for the Al alloy samples when the combination of the alkali and acid treatments (and vice versa) were employed, as seen in Table 3. Thus, contact-angle measurements confirmed that both chemical treatments improved the surface wettability of the Al alloy but to a different degree.

Table 5
Results of the elemental composition (in at.%) of the Al 2p after deconvolution for all the examined cases, determined by XPS.

Treatment	Elements		
	Al $2p_{3/2}$ metal	Al $2p_{1/2}$ metal	Al 2p oxide
Degreased-only	11.44	1.23	5.63
Alkaline (10 wt%) for 20 min	4.16	2.08	7.32
Acid for 20 min	7.46	3.73	13.98
Anodising (Def Stan 03-25/4)	1.21	0.61	2.67
Atmospheric plasma (1 scan at 1 mm/s)	0.51	0.26	3.38

Anodising is a widely used method allowing the improvement of adhesion, lubrication and protection properties of Al [20,32]. The porous morphology and highly adsorptive nature of the oxide film that results from anodisation could be critical to improve the adhesion between organic coatings applied on the etched Al alloy samples. The wettability results obtained for the anodised Al alloy were in similar range to the alkali and acid treatments with longer exposure times (Table 3). A large number of fine and uniform pores were evident on the anodised Al surface, as shown in the micrographs in Fig. 2(g) and (h).

Surface free energy measurements of the Al alloy samples treated with atmospheric pressure plasma, generated in the ambient air, were also carried out, as shown in Table 3. The plasma treated Al alloy surface exhibited a significant improvement in the surface wettability due to increased surface polarity. The oxidation of the surface and the removal of the carbonaceous components made the Al surface more hydrophilic. It is apparent, however, that when the number of scans or the speed was increased (from 1 scan to 3 scans, or from 1 mm/s to 10 mm/s) the wettability of the Al surface was decreased. Fig. 2(i) and (j) shows typical images of the Al alloy surface topography after plasma treatment. It is

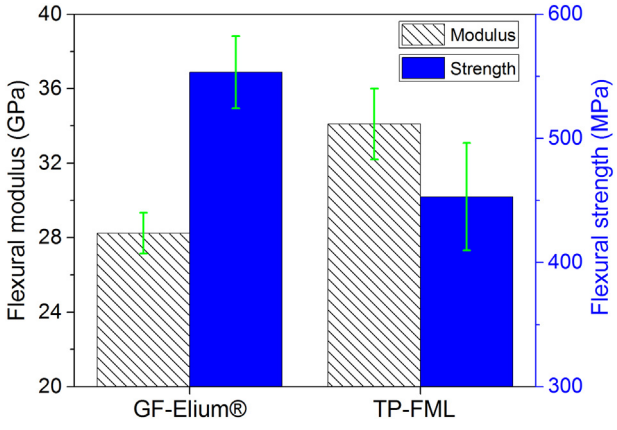

Fig. 5. Longitudinal flexural modulus (black-sparse) and strength (blue-blank) of the TP-FML and GF-Elium® cases. The flexural values are averages from ~6 tests for each case. (For interpretation of the references to color in this figure legend, the reader is referred to the web version of this article.)

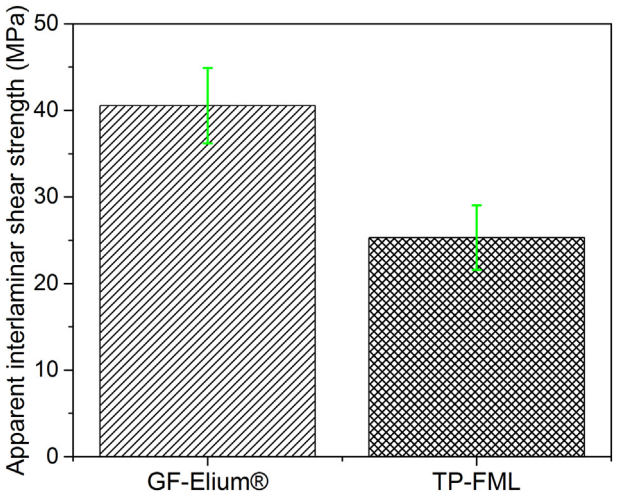

Fig. 6. Comparison of ILSS values between TP-FML and GF-Elium® specimens obtained by the short beam test method.

worth pointing out that the water contact-angles tended to increase after prolonged exposure to atmospheric conditions, which is an indication of an ageing process called "hydrophobic recovery" [33,34]. Consequently, the surface properties are time dependent.

The aforementioned findings revealed that chemical etching, anodising and plasma treatment of the Al alloy surface could effectively enhance its surface free energy and wettability but to a different degree depending on the applied experimental parameters. Park et al. reported that rough substrates are essential for enhancing joint strength, which in turn increases the energy required for crack propagation [21]. The increased surface roughness is likely to promote mechanical interlocking phenomena between the Al alloy and the matrix improving interfacial adhesion.

3.2. Chemical composition

The X-ray photoelectron spectroscopy (XPS) method was adopted to determine the chemical composition on the surface of the treated Al alloy samples. However, due to small differences between the same treatments, only the most representative XPS spectra for each treatment are presented (similar with the Section 3.1). Fig. 3 presents wide-scan spectra of the treated Al alloy sheets. In the region of binding energies up to 600 eV the spectra of the Al alloy samples contained five intensive XPS peaks including Al 2p, C 1s, O 1s. The results of the treated Al alloy's surface composition are summarized in Table 4. Note that low-intensity peaks of magnesium (Mg 2s), manganese (Mn 2p), iron (Fe 2p) and copper (Cu $2p_{3/2}$) observed in the XPS spectra of the Al alloy samples were found to be around 1–2 atomic percent (at.%) and were not further considered. The presence of these elements in the spectrum was due to the chemical composition of the Al alloy (6082-T6) used in this study (see also Table 1). Low-intensity peaks of sulphur (S 2p) and sodium (Na 1s) observed in the degreased-only and acid-etched samples were attributed to the residual impurities and/or contaminants. Furthermore, the high phosphorus (P 2s) concentration at around 5.43 at.% resulted from the anodising-cleaning in the acid bath. The presence of calcium (Ca 2p) in the spectra might have originated from the water used to clean the chemically treated samples, but the source of fluorine (F 1s) revealed for the degreased-only case was unclear. Overall, in all cases, the control spectra consisted of two large peaks at ~531 and ~285 eV resulting from oxygen and carbon presence on the surface, respectively.

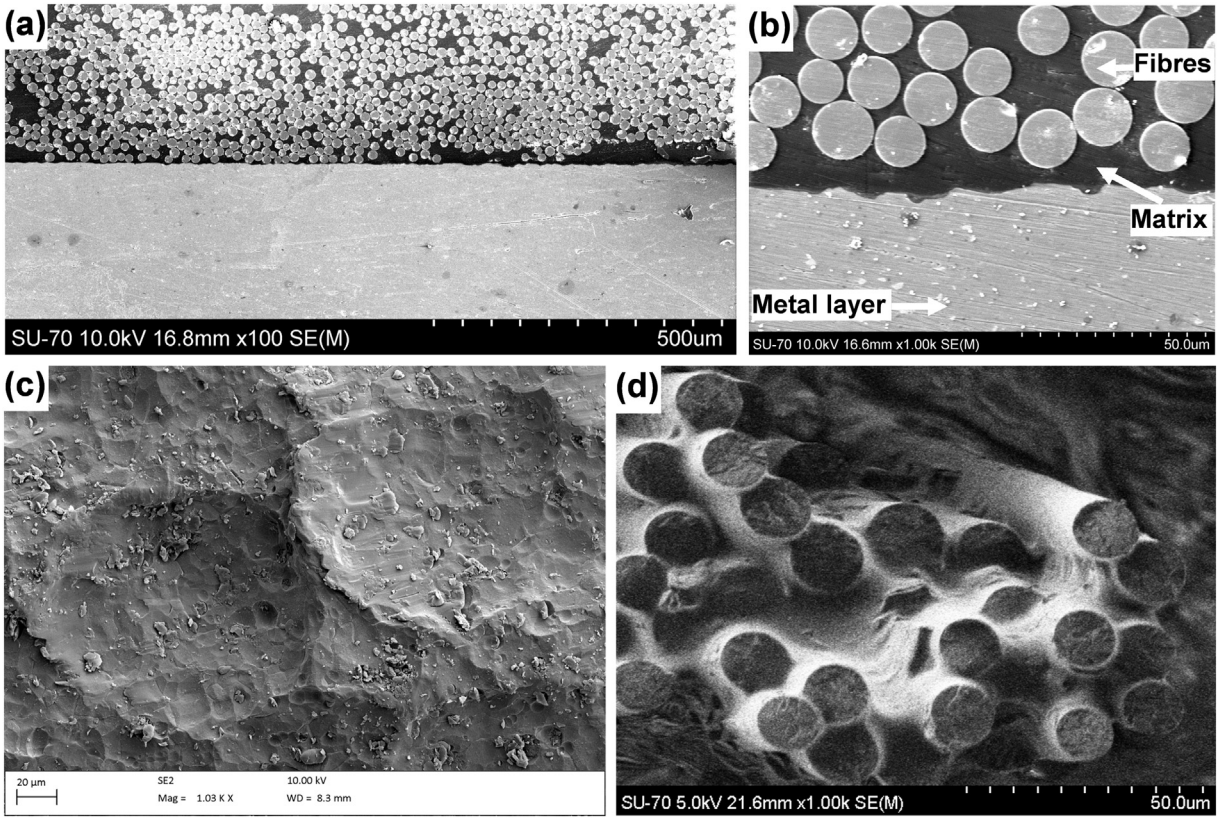

Fig. 7. (a) Low and (b) high magnification SEM micrographs taken at the composite/Al alloy interface. (c) Debonded Al alloy surface after flexural testing. (d) Flexural/fractured surface of the GF-Elium® under bending mode.

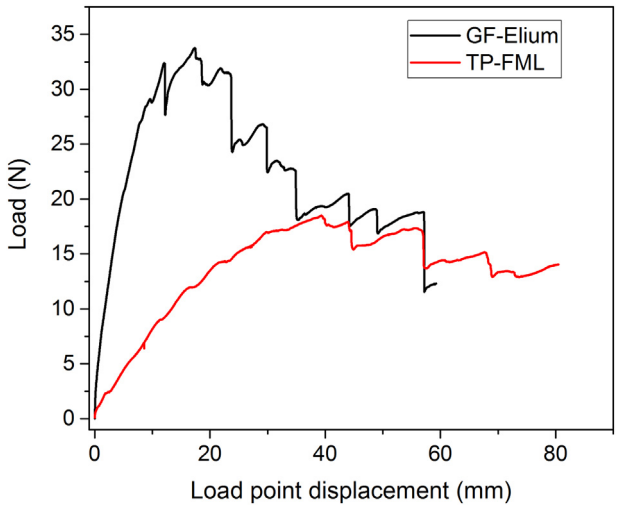

Fig. 8. Representative load–displacement curves of the GF-Elium® and the TP-FML.

An additional peak was evident at low binding energies indicating the presence of Al at ~73 eV [32,35–37]. The latter demonstrated that reliable scans were acquired without significant charging on the Al alloy surface in agreement with the literature [25,36–39]. In all cases, the reduction of the carbon (C 1s) amount in atomic percent (at.%) on the Al surface was evident owing to the applied treatments (Table 4). The atomic fraction of carbon on the surface of the degreased-only Al alloy sample was ~72%, which was reduced to ~32% after the alkaline etching, to ~26% after acid treatment, to ~29% after anodisation and to 48% after atmospheric plasma treatment. Oxidation of the Al alloy surface was evident from the increase in the oxygen O 1s peak area after the surface modifications. In addition, the effect of the treatments was clearly observed by the increased Al amount (Table 4) and subsequently by the increased intensity of Al 2p peaks (Fig. 3). The small reduction of the C 1 s orbital peak in the plasma treated sample could be explained by the re-adsorption of hydrocarbon-impurities (sticking of volatile organic compounds, VOC) from the surrounding atmosphere, because of the very hydrophilic character of the Al surface after plasma treatment. Moreover, a fraction of the plasma-treated Al surface is likely to get hydrated due to the atmospheric conditions [40–42]. Even though the chemically treated samples were dried (using nitrogen) and sealed in polyethylene bags immediately after rinsing, oxidation (and slight hydration) of the surfaces cannot be avoided due to the strong chemical affinity of Al towards oxygen. Thus, in the presence of moisture, the oxygen surface atoms were replaced by hydroxyl groups (OH) which might have an effect on the properties of the oxide layers, hence on the wetting behaviour of the Al alloys.

Fig. 4 shows high-resolution XPS spectra of Al 2p for the examined Al alloys. All the spectra were de-convoluted into two distinct peaks, indicating the presence of metallic Al and oxidized Al at binding energy from ~72 to ~73 eV and from ~73 to ~75 eV, respectively [35,36,43]. Additionally, the Al 2p core level can be decomposed into the lower binding energy peaks at 72.3 ± 0.2 and at 72.8 ± 0.1 eV assigned to the Al $2p_{3/2}$ and Al $2p_{1/2}$ spin orbit doublet of metallic Al, as displayed in Fig. 4 [27,35]. The Full Width at Half Maximum (FWHM) of the Al $2p_{1/2}$ spin orbit component is larger than that of Al $2p_{3/2}$, and the Al $2p_{1/2}$: Al $2p_{3/2}$ area ratio is 0.50 ± 0.05, which is consistent with the theoretical value [35,44]. The separation distance between the two Al 2p metal peaks is known to differ, depending on the thickness of the oxide layer [40,43]. In addition, Table 5 shows the results from the deconvolution of the Al 2p peaks for all the cases. Assuming an ideal layer, the thickness of this oxide film can be determined from the relative intensities of the Al 2p (oxide) peak and the Al 2p (metal) peaks. A detailed analysis of the oxide film thickness on the surface can be done using the model established by Carlson [45] and Strohmeier [40]:

$$d_{\mathrm{Al\ 2p}}(\mathrm{nm}) = \lambda_{ox} \cdot \sin\theta \cdot \ln\left(\frac{N_m \cdot \lambda_m \cdot I_{ox}}{N_{ox} \cdot \lambda_{ox} \cdot I_m} + 1\right) \quad (7)$$

where $d_{\mathrm{Al\ 2p}}$ (nm) is the thickness of the oxide layer, θ is the photoelectron take-off angle (measured from the sample surface), I_{ox} and I_m are the percentage areas of the oxide and metal peaks fitted from the high-resolution spectrum, λ_m and λ_{ox} are the inelastic mean free paths of the photoelectron for the metal and oxide. N_m and N_{ox} are the volume densities of the metal atoms in the metal and oxide. The volume density for both metal and oxide is the respective density divided by the molar mass of each compound. The inelastic mean free paths λ_m and λ_{ox} was determined, using the NIST Standard Reference Database 81 [46], to be 2.39 and 2.92 nm, respectively. These values are specific to Al 2p photoelectrons generated using Al Kα radiation emitted normal to the surface ($\theta = 90°$) of the ESCA300 instrument, which has an angle of 45° between the x-ray source and the axis of the electron lens. Hence, the oxide layer $d_{\mathrm{Al\ 2p}}$ of the degreased-only Al sample was 3.12 nm, for the alkali-treated and the acid-etched cases was calculated at 2.71 nm and 2.92 nm, respectively. For the anodised and plasma treated Al alloy samples the thickness of the oxide layer was estimated to be at 13.8 and 5.5 nm, respectively.

Summarising the aforementioned results, XPS data revealed that changes in wettability were attributed to the decreased amount of the atomic carbon and the increased amount of the Al oxide as well as the promoted oxidation effect on the Al surface. Since aromatic carbon layers (graphite) are characterised by hydrophobic behaviour, the edges of carbon layers need to satisfy their valence electron, therefore many moieties can be found there. As far as these moieties are oxygenated (after surface treatments), the carbon support becomes hydrophilic. Hence, in our cases, the reduction of the amount of the carbon and subsequent oxidation resulted in more hydrophilic surface in agreement with the wettability measurements. Moreover, the presence of metallic Al, the improved lubrication and adhesion of the surface due to the formation of micro pores might have led to an increased surface energy, although the surface roughness was increased. Consequently, the wetting behaviour of the chemically and physically treated Al surfaces was enhanced. As mentioned above, however, the effect of hydration on the oxide layer due to the atmospheric conditions could be considered to have an effect on the surface thus limiting the process of improving the wetting behaviour of the surfaces [41,42].

3.3. Flexural tests

The criteria for down-selection of the optimum metal treatment method for the production of the test TP-FMLs were surface roughness and wettability (see Table 3). Complementary qualitative bond strength testing was also performed. Manufactured TP-FML samples containing a

Table 6
Mode I interlaminar fracture toughness G_{IC} values according to ASTM D5528-13. Note that the average values were obtained from the experimental results of around 7 samples for each case.

Material	Lay-up	Al thickness (mm)	G_{IC} (J/m^2)
GF-Elium®	(4) (UD glass-fabric-Elium®)	–	2055 ± 155
TP-FML (alkali)	(1/2) (Al/UD glass-fabric-Elium®)	0.71	442 ± 105
FML (alkali) [26]	(1/1) (Al/glass-epoxy)	1.5	131 ± 3

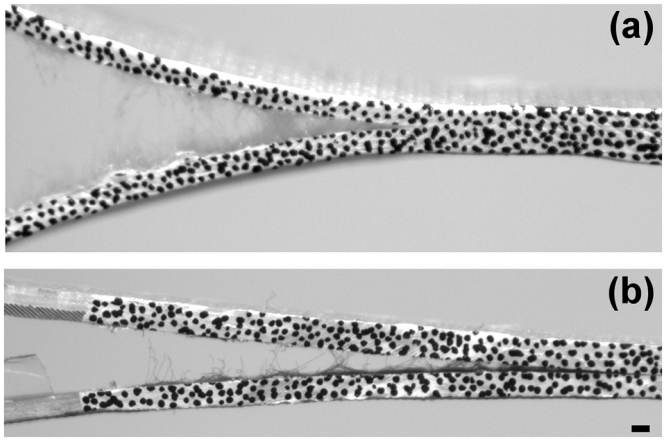

Fig. 9. Typical high-speed images of the crack tip zone for the (a) GF-Elium® and (b) TP-FMLs. The scale bar depicts a width of 1 mm.

pre-crack area (~20 mm) at the interface between the Al alloy and the composite, were pulled off (delaminated) and a relative force value was measured using a newton meter. Alkaline etching, 10 wt% for 20 min, as per the aforementioned parameters, was found to provide the best bonding by qualitative inspections with the highest resistance force of ~30–40 N. This also correlated with the measured surface properties. Following the successful VaRTM manufacturing of the TP-FMLs, extraction of the test coupons using a CNC machine was performed for preliminary flexural characterisations.

The flexural results for the TP-FML with alkali treated Al alloy and GF-Elium® composites are plotted in Fig. 5. The measured flexural strength for the baseline GF-Elium® composite (~553 MPa) was slightly higher (+18%) than that observed for the TP-FML (~452 MPa) which can be attributed to the reduced load transfer between the two dissimilar materials i.e. the Al alloy and the composite layers. The flexural modulus for the TP-FML (~34 GPa) was found to be higher (+20%) than that of the baseline GF-Elium® composite (~28 GPa), as displayed in Fig. 5. Since, both examined cases had similar type of reinforcement: UD E-glass fibres, based on the same matrix (Elium®), the differences observed in the flexural modulus were associated with the metal phase (Al 6082-T6 modulus of elasticity ~70GPa), which in turn resulted in different interfacial bond strength between the fibres/matrix and between composite/Al alloy layers. The flexural values observed for the TP-FMLs indicated an acceptable level of interfacial bonding between the composite and the Al alloy which played an important role in the ultimate performance of the TP-FML and shows promise for further future investigations.

3.4. ILSS tests

Interfacial adhesion between fibres and matrix has been reported from numerous experimental studies to have a strong influence on the interlaminar performance of composites [47]. In the present study, a comparison of the interlaminar shear strength between the GF-Elium® and the TP-FML was performed, as shown in Fig. 6. The interlaminar shear strength of the TP-FML was found to be lower (−40%) than that of the GF-Elium®. As expected, the observed behaviour in the TP-FML can be explained by the different physicochemical interactions at the metal-composite interface in comparison to the fibre/matrix interface in the GF-Elium®. It is worth pointing out that the shear force, which tends to produce a sliding failure in a material along a plane that is parallel to the direction of the force, was primarily acting at the interface between the Al alloy and the composite, in the TP-FML, during this test. On the contrary, the shear force for the GF-Elium® was acting between the composite layers.

3.5. Microscopic characteristics

Mechanical properties of TP-FMLs are inextricably linked to their (micro) structure and the macroscopically observed failure characteristics are closely connected to the microscopic fracture mechanisms. Fig. 7 (a) and (b), presents SEM micrographs taken of a typical cross section of the alkali-treated TP-FMLs at low and high magnifications, respectively. The composite/Al alloy interface, the absence of visible voids, as well as the boundaries between the fibre/matrix and the composite/metal can be seen clearly. Note that the SEM micrographs show the glass fibres at 0° orientation. The examined TP-FML and GF-Elium® samples revealed high consolidation quality with no visible voids. Moreover, representative SEM images of the debonded and fracture surfaces for the TP-FML and the GF-Elium® cases, tested in flexure, are shown in Fig. 7 (c) and (d), respectively. The presence of craters (as discussed in Section 3.1) were observed on the delaminated Al alloy surface where resin remnants were evident indicating a good bonding between the composite and the Al alloy layers (Fig. 7c). In Fig. 7(d), a SEM micrograph of the fractured GF-Elium® sample indicated fully wetted glass fibres with excellent fibre/matrix adhesion property.

3.6. Interlaminar fracture toughness test

The interlaminar fracture toughness was determined for the TP-FML and the GF-Elium® in terms of Mode-I critical strain energy release rate

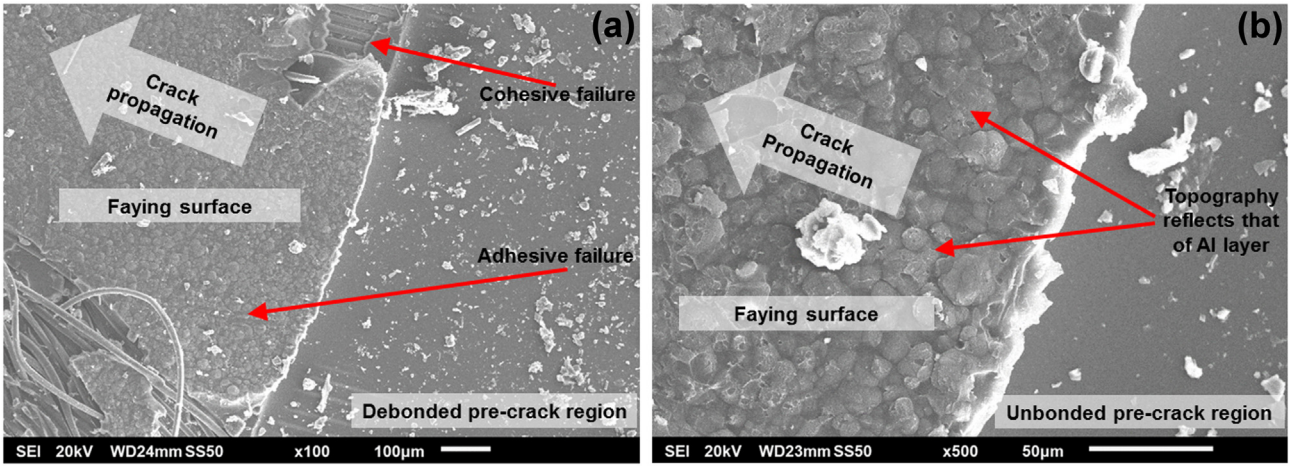

Fig. 10. (a) Low and (b) high magnification SEM micrographs showing the composite faying surface of the TP-FML, after DCB testing.

(per unit area), which may be regarded as G_{IC}. The crack length and apparent G_{IC} values were obtained from the high-speed image sequences of each interlaminar fracture toughness test, which recorded at ~1000 frames per second. Typical load–displacement curves from the interlaminar fracture tests are shown in Fig. 8. The load increased linearly in both the cases until it reached a maximum value where the crack initiated (at around ~63 mm), and then a gradual decrease of the load was evident with the increase in crack propagation. Characteristic stick-slip behaviour for GF-Elium® and TP-FML was observed due to the variations in local material properties, such as resin-rich or fibre-rich regions along the longitudinal direction, misalignment of the fibres and presence of voids, the fracture of bridged fibres or fibre bundles, as well as level of adhesion or bonding between composite/Al alloy. For the GF-Elium® case, the load abruptly dropped at several points after the peak load corresponding to an unstable and intensive crack propagation mechanism. The latter is a distinctive fracture behaviour of composite (FRP) materials using the DCB method, as reported in previous studies [48–52]. On the contrary, TP-FML followed a more stable and slow crack propagation, characterised by smaller drops in load [13,26,53]. The crack was observed to propagate in the main delamination plane without any side cracking and branching. Both curves exhibited repetitive load drops followed by a gradual increase of the load. The curves in Fig. 8 show that the load needed to initiate delamination was clearly greater for the GF-Elium® than the TP-FML case. Furthermore, a decrease in stiffness can be observed for the TP-FML case (Fig. 8), which was attributed to the interface between composite/Al alloy. The resistance to deform in response to the applied force was represented by the slope of the load–displacement curves in each case. It is important to note that the presence of the drilled holes on the Al alloy surface could effectively increase the overall surface roughness of the metal layer which in turn might enhance the fracture resistance of the composite/Al alloy at the interface and subsequently increase the strain energy release rate (G_{IC}) [26,54,55].

It is well known that the interlaminar fracture toughness test (Double Beam Cantilever test or DCB test) is performed on symmetrical and homogeneous composites and the critical strain energy released during the DCB test can be interpreted as pure Mode I or Mode II loading condition. However, in the case of FMLs, the co-existence of dissimilar materials with different physical and mechanical properties are likely to affect the ultimate fracture resistance of the hybrid composite. In addition, FML specimens under interlaminar fracture toughness test will always be characterised by asymmetry as the initial delamination is situated at the composite/Al alloy interface [56–58]. Thus, TP-FML testing by the DCB method will be defined as mode mixity at the crack tip [56–58]. More specifically, in our TP-FML case, the bending stiffness difference between the composite/Al alloy side and the composite side resulted in the contribution of Mode II in the fracture mechanism. However, as reported by Mollón et al. [59], and Sebaey et al. [60], the Mode II fracture contribution due to the asymmetric crack propagation during DCB test was found to be negligible when compared to Mode I.

The results of the Mode-I interlaminar fracture toughness tests are summarized in Table 6. The G_{IC} values refer to averages obtained from the strain energy released during crack initiation and propagation according to ASTM D5528-13 (MBT). The overall interlaminar fracture toughness values of GF-Elium® ($G_{IC} \approx 2055$ J/m^2) was higher than that in the TP-FML ($G_{IC} \approx 442$ J/m^2), which simply means that GF-Elium® composite exhibits a higher crack propagation resistance than an equivalent TP-FML. However, the G_{IC} obtained for TP-FML ($\approx$442 J/m^2) in this study, exceeds the G_{IC} value of the thermoset FMLs ($\approx$131 J/m^2) reported by Laban et al. with alkali treated Al alloy [26]. Given that, Laban et al. studied an epoxy-based FML and that bonding of the epoxy resins (thermosets) with the Al alloy is well established, the superior interlaminar fracture toughness performance of the Elium®-FML (thermoplastic-based) is promising. This indicates an acceptable level of interfacial bonding between the Al alloy and the composite layer occurred.

Fig. 9 shows typical high-speed images of the two cases during testing. Both materials exhibited distinctive delamination features, which reflected the initiation and propagation mechanisms of the tested samples and thus the resistance to fracture. As expected, fibre bridging was prominent in the GF-Elium®. Remarkably, some fibre bridging was also observed in the TP-FML, which is indicative of strong interfacial bonding.

SEM micrographs of the representative fracture surfaces after interlaminar fracture toughness testing are shown in Fig. 10. It is clear from the fracture surface morphology of the TP-FML sample that an optimum level of composite/Al alloy interfacial bonding was achieved. A mixed failure mode was observed including both adhesive and cohesive failures. The latter was due to the surface roughness of the treated-Al sheets, which resulted in a non-uniform crack propagation mechanism. The regions of adhesive failure showed imprints of the treated Al substrate, as discussed in Section 3.1, which is indicative of good bonding.

4. Conclusions

This study investigated the effect of various treatments on the surface characteristics of an Al alloy for manufacturing thermoplastic fibre-metal laminates by resin infusion. Chemical and electrochemical etching as well as physical etching (plasma exposure) were employed to activate the Al alloy surface, prior to TP-FML fabrication. Parameters such as the etchant type and the treatment time were extensively examined. Multiple characterisation techniques were adopted including profilometry, interferometry and contact-angle goniometry. All applied treatments improved the wetting behaviour of the Al alloy surface but in a varying degree (+60% to +30%) depending on the applied experimental parameters (Table 3). The improved wettability was shown to enhance the adhesion properties of the treated Al alloy surfaces and in turn, the interfacial bonding of composite/Al alloy layers. Furthermore, the chemical composition of Al alloy surface was determined, before and after the treatments, using the XPS method. The surface activation, cleaning and etching of the Al alloy samples were evident in the form of decreased amount of carbonaceous compounds and the increased amount of oxygen species, hydroxides and oxyhydroxides (Tables 4 and 5), hence resulting in a more hydrophilic surface. Overall, the enhancement of Al alloy wettability combined with the surface roughness was found to be necessary to achieve good adhesion between the Al alloy and the composite layer. Suitable surface treatment conditions: 10 wt% NaOH for 20 min, of the Al alloy sheets were identified for the production of TP-FMLs.

Following the successful VaRTM manufacturing of fully-wetted TP-FMLs with good interfacial bonding, mechanical characterisation was performed along with the optical characteristics of the tested/failed hybrid composites. Longitudinal flexural and short beam shear tests were conducted on TP-FMLs and compared to the baseline GF-Elium® case. The flexural strength of the GF-Elium® was found to be +10% higher than the TP-FML while the flexural stiffness was −23% lower than the TP-FML owing to the dissimilar lay-up and the high modulus of elasticity of the Al alloy layer, respectively. The interlaminar shear strength of the GF-Elium® was +41% higher than the TP-FML which was attributed to the different shear forces acting across the layers of the two cases. Moreover, the interlaminar fracture toughness of the manufactured TP-FML was evaluated. The adopted Al surface treatment in relation to the matrix (Elium®) properties resulted in a strong composite/Al alloy interface, which was characterised by remarkably higher fracture resistance and strain released energy compared to other reported studies on FMLs. In summary, the overall mechanical performance of the manufactured alkali-treated TP-FMLs demonstrated that an acceptable level of interfacial bonding was achieved, and the measured properties were in a comparable range with properties published in the literature. A novel way of bonding Al alloy sheets and thermoplastic composite layers through the in-situ polymerisation technique was found to be

successful with promising potential on the industrial viability of this technology.

CRediT authorship contribution statement

Dimitrios Mamalis: Conceptualization, Funding acquisition, Methodology, Project administration, Supervision, Validation, Writing - original draft, Writing - review & editing. **Winifred Obande:** Data curation, Formal analysis, Software, Visualization, Methodology, Validation, Writing - review & editing. **Vasileios Koutsos:** Funding acquisition, Conceptualization, Investigation, Resources, Supervision, Validation, Writing - review & editing. **Jane R. Blackford:** Conceptualization, Investigation, Resources, Supervision, Validation, Writing - review & editing. **Conchúr M. Ó Brádaigh:** Funding acquisition, Conceptualization, Investigation, Resources, Supervision, Validation, Writing - review & editing. **Dipa Ray:** Funding acquisition, Conceptualization, Investigation, Resources, Methodology, Project administration, Supervision, Validation, Writing - original draft, Writing - review & editing.

Acknowledgments

This work was supported by the Engineering and Physical Sciences Research Council [grant number: EP/P006701/1], through the CIMComp, EPSRC Future Composites Manufacturing Research Hub. The authors would like to thank ARKEMA for the material supply and the support. The authors are also thankful to the Manufacturing Metrology Team at the University of Nottingham, for performing a series of optical surface tests. XPS data collection was performed at the EPSRC National Facility for XPS ('HarwellXPS'), operated by Cardiff University and UCL, under contract No. PR16195.

References

[1] I. Ortiz de Mendibil, L. Aretxabaleta, M. Sarrionandia, M. Mateos, J. Aurrekoetxea, Impact behaviour of glass fibre-reinforced epoxy/aluminium fibre metal laminate manufactured by Vacuum Assisted Resin Transfer Moulding, Compos. Struct. 140 (2016) 118–124, https://doi.org/10.1016/J.COMPSTRUCT.2015.12.026.
[2] N. Tsartsaris, M. Meo, F. Dolce, U. Polimeno, M. Guida, F. Marulo, Low-velocity impact behavior of fiber metal laminates, J. Compos. Mater. 45 (2011) 803–814, https://doi.org/10.1177/0021998310376108.
[3] T. Sinmazçelik, E. Avcu, M.Ö. Bora, O. Çoban, A review: fibre metal laminates, background, bonding types and applied test methods, Mater. Des. 32 (2011) 3671–3685, https://doi.org/10.1016/j.matdes.2011.03.011.
[4] R.R. Kulkarni, K.K. Chawla, U.K. Vaidya, M.C. Koopman, A.W. Eberhardt, Characterization of long fiber thermoplastic/metal laminates, J. Mater. Sci. 43 (2008) 4391–4398, https://doi.org/10.1007/s10853-007-2437-5.
[5] M.R. Abdullah, Y. Prawoto, W.J. Cantwell, Interfacial fracture of the fibre-metal laminates based on fibre reinforced thermoplastics, Mater. Des. 66 ((2015) 446–452, https://doi.org/10.1016/J.MATDES.2014.03.058.
[6] M.R. Abdullah, W.J. Cantwell, The impact resistance of polypropylene-based fibre–metal laminates, Compos. Sci. Technol. 66 (2006) 1682–1693, https://doi.org/10.1016/J.COMPSCITECH.2005.11.008.
[7] P. Cortés, W.J. Cantwell, Structure–properties relations in titanium-based thermoplastic fiber–metal laminates, Polym. Compos. 27 (2006) 264–270, https://doi.org/10.1002/pc.20189.
[8] Y. Hu, H. Li, X. Fu, X. Zhang, J. Tao, J. Xu, Hygrothermal characterization of polyimide-titanium-based fibre metal laminate, Polym. Compos. 39 (2018) 2819–2825, https://doi.org/10.1002/pc.24274.
[9] Y. Hu, H. Li, J. Tao, L. Pan, J. Xu, The effects of temperature variation on mechanical behaviors of polyetheretherketone-based fiber metal laminates, Polym. Compos. 39 (2018) 1447–1454, https://doi.org/10.1002/pc.24085.
[10] Q. Lin, M. Ferriol, M. Cochez, H. Vahabi, C. Vagner, Continuous fiber-reinforced thermoplastic composites: influence of processing on fire retardant properties, Fire Mater. 41 (2017) 646–653, https://doi.org/10.1002/fam.2406.
[11] Thermoplastic resins Elium® for composite parts, https://www.arkema.com/en/products/product-finder/range-viewer/Elium-resins-for-composites 2018.
[12] D.S. Cousins, Y. Suzuki, R.E. Murray, J.R. Samaniuk, A.P. Stebner, Recycling glass fiber thermoplastic composites from wind turbine blades, J. Clean. Prod. 209 (2018) 1252–1263, https://doi.org/10.1016/J.JCLEPRO.2018.10.286.
[13] S.K. Bhudolia, P. Perrotey, S.C. Joshi, Mode I fracture toughness and fractographic investigation of carbon fibre composites with liquid methylmethacrylate thermoplastic matrix, Compos. Part B Eng. 134 (2018) 246–253, https://doi.org/10.1016/j.compositesb.2017.09.057.
[14] P. Davies, M. Arhant, Fatigue behaviour of acrylic matrix composites: influence of seawater, Appl. Compos. Mater. (2018) 1–12, https://doi.org/10.1007/s10443-018-9713-1.
[15] S.K. Bhudolia, P. Perrotey, S.C. Joshi, Enhanced vibration damping and dynamic mechanical characteristics of composites with novel pseudo-thermoset matrix system, Compos. Struct. 179 (2017) 502–513, https://doi.org/10.1016/J.COMPSTRUCT.2017.07.093.
[16] P. Davies, P.-Y. Le Gac, M. Le Gall, Influence of sea water aging on the mechanical behaviour of acrylic matrix composites, Appl. Compos. Mater. 24 (2017) 97–111, https://doi.org/10.1007/s10443-016-9516-1.
[17] A. Chilali, W. Zouari, M. Assarar, H. Kebir, R. Ayad, Analysis of the mechanical behaviour of flax and glass fabrics-reinforced thermoplastic and thermoset resins, J. Reinf. Plast. Compos. 35 (2016) 1217–1232, https://doi.org/10.1177/0731684416645203.
[18] A. Chilali, W. Zouari, M. Assarar, H. Kebir, R. Ayad, Effect of water ageing on the load-unload cyclic behaviour of flax fibre-reinforced thermoplastic and thermosetting composites, Compos. Struct. 183 (2018) 309–319, https://doi.org/10.1016/J.COMPSTRUCT.2017.03.077.
[19] S.K. Bhudolia, P. Perrotey, S.C. Joshi, Mode I fracture toughness and fractographic investigation of carbon fibre composites with liquid methylmethacrylate thermoplastic matrix, Compos. Part B Eng. 134 (2018) 246–253, https://doi.org/10.1016/J.COMPOSITESB.2017.09.057.
[20] A. Bjørgum, F. Lapique, J. Walmsley, K. Redford, Anodising as pre-treatment for structural bonding, Int. J. Adhes. Adhes. 23 (2003) 401–412, https://doi.org/10.1016/S0143-7496(03)00071-X.
[21] S.Y. Park, W.J. Choi, H.S. Choi, H. Kwon, Effects of surface pre-treatment and void content on GLARE laminate process characteristics, J. Mater. Process. Technol. 210 (2010) 1008–1016, https://doi.org/10.1016/J.JMATPROTEC.2010.01.017.
[22] M.S. Islam, L. Tong, P.J. Falzon, Influence of metal surface preparation on its surface profile, contact angle, surface energy and adhesion with glass fibre prepreg, Int. J. Adhes. Adhes. 51 (2014) 32–41, https://doi.org/10.1016/J.IJADHADH.2014.02.006.
[23] T.S.M. Mui, L.L.G. Silva, V. Prysiazhnyi, K.G. Kostov, Surface modification of aluminium alloys by atmospheric pressure plasma treatments for enhancement of their adhesion properties, Surf. Coat. Technol. 312 (2017) 32–36, https://doi.org/10.1016/J.SURFCOAT.2016.08.024.
[24] S. Sharifi Golru, M.M. Attar, B. Ramezanzadeh, Effects of surface treatment of aluminium alloy 1050 on the adhesion and anticorrosion properties of the epoxy coating, Appl. Surf. Sci. 345 (2015) 360–368, https://doi.org/10.1016/J.APSUSC.2015.03.148.
[25] N.G. Gonzalez-Canche, E.A. Flores-Johnson, P. Cortes, J.G. Carrillo, Evaluation of surface treatments on 5052-H32 aluminum alloy for enhancing the interfacial adhesion of thermoplastic-based fiber metal laminates, Int. J. Adhes. Adhes. 82 (2018) 90–99, https://doi.org/10.1016/J.IJADHADH.2018.01.003.
[26] O. Laban, E. Mahdi, Enhancing mode I inter-laminar fracture toughness of aluminum/fiberglass fiber-metal laminates by combining surface pre-treatments, Int. J. Adhes. Adhes. 78 (2017) 234–239, https://doi.org/10.1016/J.IJADHADH.2017.08.008.
[27] T.S. Williams, H. Yu, R.F. Hicks, Atmospheric pressure plasma activation as a surface pre-treatment for the adhesive bonding of aluminum 2024, J. Adhes. Sci. Technol. 28 (2014) 653–674, https://doi.org/10.1080/01694243.2013.859646.
[28] Wilsons Ltd, Supplier datasheet, http://www.wilsonsmetals.com/datasheets/?gId=1&sgId=36 2018.
[29] Ministry of Defence, Defence Standard 03-25 (Sulfuric Acid Anodising of Aluminium and Aluminium Alloys), 2003.
[30] M.E. Schrader, Young-Dupre revisited, Langmuir 11 (1995) 3585–3589, https://doi.org/10.1021/la00009a049.
[31] D. Li, A.. Neumann, A reformulation of the equation of state for interfacial tensions, J. Colloid Interface Sci. 137 (1990) 304–307, https://doi.org/10.1016/0021-9797(90)90067-X.
[32] P.G. Sheasby, R. Pinner, S. Wernick, The Surface Treatment and Finishing of Aluminium and Its Alloys, ASM International, 2001.
[33] V. Prysiazhnyi, Atmospheric pressure plasma treatment and following aging effect of chromium surfaces, J. Surf. Eng. Mater. Adv. Technol. 03 (2013) 138–145, https://doi.org/10.4236/jsemat.2013.32018.
[34] V. Prysiazhnyi, V. Zaporojchenko, H. Kersten, M. Černák, Influence of humidity on atmospheric pressure air plasma treatment of aluminium surfaces, Appl. Surf. Sci. 258 (2012) 5467–5471, https://doi.org/10.1016/J.APSUSC.2012.02.040.
[35] B.V. Crist, A review of XPS data-banks, XPS Rep. 1 (2007) 1–52http://www.xpsdata.com/JAXR_2007/A_Review_of_XPS_Data-banks_BVC.pdf.
[36] L. Bónová, A. Zahoranová, D. Kováčik, M. Zahoran, M. Mičušík, M. Černák, Atmospheric pressure plasma treatment of flat aluminum surface, Appl. Surf. Sci. 331 (2015) 79–86, https://doi.org/10.1016/J.APSUSC.2015.01.030.
[37] S. Klingner, F. Voigts, W. Viöl, W. Maus-Friedrichs, Analysis of plasma degreased aluminium foil with XPS, Surf. Eng. 29 (2013) 396–401, https://doi.org/10.1179/1743294413Y.0000000129.
[38] M.C. Kim, S.H. Yang, J.-H. Boo, J.G. Han, Surface treatment of metals using an atmospheric pressure plasma jet and their surface characteristics, Surf. Coat. Technol. 174–175 (2003) 839–844, https://doi.org/10.1016/S0257-8972(03)00560-7.
[39] B. Luan, T. Le, J. Nagata, An investigation on the coating of 3003 aluminum alloy, Surf. Coat. Technol. 186 (2004) 431–443, https://doi.org/10.1016/J.SURFCOAT.2003.12.031.
[40] B.R. Strohmeier, An ESCA method for determining the oxide thickness on aluminum alloys, Surf. Interface Anal. 15 (1990) 51–56, https://doi.org/10.1002/sia.740150109.
[41] G. Lefèvre, M. Duc, P. Lepeut, R. Caplain, M. Fédoroff, Hydration of γ-alumina in water and its effects on surface reactivity, Langmuir 18 (2002) 7530–7537, https://doi.org/10.1021/la025651i.
[42] B.C. Bunker, G.C. Nelson, K.R. Zavadil, J.C. Barbour, F.D. Wall, J.P. Sullivan, C.F. Windisch Jr, M.H. Engelhardt, D.R. Baer, Hydration of Passive Oxide Films on Aluminum, (n.d.). doi:https://doi.org/10.1021/jp013246e.

[43] C. Ocal, B. Basurco, S. Ferrer, An ISS-XPS study on the oxidation of Al(111); identification of stoichiometric and reduced oxide surfaces, Surf. Sci. 157 (1985) 233–243, https://doi.org/10.1016/0039-6028(85)90645-4.
[44] N. Chen, C. Wang, J. Hwang, F. Huang, MOCVD Al nanocrystals embedded in AlOxNy thin films for nonvolatile memory, ECS J. Solid State Sci. Technol. 1 (2012) P190–P196, https://doi.org/10.1149/2.018204jss.
[45] T.A. Carlson, G.E. McGuire, Study of the X-ray photoelectron spectrum of tungsten–tungsten oxide as a function of thickness of the surface oxide layer, J. Electron Spectrosc. Relat. Phenom. 1 (1972) 161–168, https://doi.org/10.1016/0368-2048(72)80029-X.
[46] C.J. Powell, A. Jablonski, NIST Standard Reference Database 82 NIST Electron Effective-Attenuation-Length Database, Gaithersburg, Maryland https://www.nist.gov/sites/default/files/documents/srd/SRD82UsersGuideV1-3.pdf 2011.
[47] M. Sharma, S. Gao, E. Mäder, H. Sharma, L.Y. Wei, J. Bijwe, Carbon fiber surfaces and composite interphases, Compos. Sci. Technol. 102 (2014) 35–50, https://doi.org/10.1016/j.compscitech.2014.07.005.
[48] K. Friedrich, Microstructural efficiency and fracture toughness of short fiber/thermoplastic matrix composites, Compos. Sci. Technol. 22 (1985) 43–74, https://doi.org/10.1016/0266-3538(85)90090-9.
[49] H. Wittich, M. Evstatiev, E. Bozwelieva, K. Friedrich, S. Fakirov, Effect of crystallinity on the interlaminar fracture toughness of continuous glass fiber-polyamide composites, Adv. Compos. Mater. 2 (1992) 135–152, https://doi.org/10.1163/156855192X00161.
[50] A.P. Mouritz, C. Baini, I. Herszberg, Mode I interlaminar fracture toughness properties of advanced textile fibreglass composites, Compos. A: Appl. Sci. Manuf. 30 (1999) 859–870, https://doi.org/10.1016/S1359-835X(98)00197-3.
[51] Y. Wang, Q. Dong, X. Liu, Mode 1 Interlaminar fracture behaviour of continuous glass fibre/polypropylene composites based on commingled yarn, Polym. Polym. Compos. 15 (2007) 229–239, https://doi.org/10.1177/096739110701500307.
[52] S. Mathurosemontri, K. Okuno, Y. Ogura, S. Thumsorn, H. Hamada, Investigation on fracture behavior of glass fiber reinforced thermoplastic and thermosetting composites, Key Eng. Mater. 728 (2017) 235–239, https://doi.org/10.4028/www.scientific.net/KEM.728.235.
[53] X. Zhang, Q. Ma, Y. Dai, F. Hu, G. Liu, Z. Xu, G. Wei, T. Xu, Q. Zeng, W. Xie, Effects of surface treatments and bonding types on the interfacial behavior of fiber metal laminate based on magnesium alloy, Appl. Surf. Sci. 427 (2018) 897–906, https://doi.org/10.1016/J.APSUSC.2017.09.024.
[54] H.C. Man, K.Y. Chiu, X. Guo, Laser surface micro-drilling and texturing of metals for improvement of adhesion joint strength, Appl. Surf. Sci. 256 (2010) 3166–3169, https://doi.org/10.1016/J.APSUSC.2009.11.092.
[55] J. Byskov-Nielsen, P. Balling, Laser structuring of metal surfaces: micro-mechanical interlocking, Appl. Surf. Sci. 255 (2009) 5591–5594, https://doi.org/10.1016/J.APSUSC.2008.07.118.
[56] J. Bieniaś, K. Dadej, B. Surowska, Interlaminar fracture toughness of glass and carbon reinforced multidirectional fiber metal laminates, Eng. Fract. Mech. 175 (2017) 127–145, https://doi.org/10.1016/J.ENGFRACMECH.2017.02.007.
[57] V. Sundararaman, B.D. Davidson, An unsymmetric end-notched flexure test for interfacial fracture toughness determination, Eng. Fract. Mech. 60 (1998) 361–377, https://doi.org/10.1016/S0013-7944(98)00017-4.
[58] F. Ducept, D. Gamby, P. Davies, A mixed-mode failure criterion derived from tests on symmetric and asymmetric specimens, Compos. Sci. Technol. 59 (1999) 609–619, https://doi.org/10.1016/S0266-3538(98)00105-5.
[59] V. Mollón, J. Bonhomme, J. Viña, A. Argüelles, Theoretical and experimental analysis of carbon epoxy asymmetric dcb specimens to characterize mixed mode fracture toughness, Polym. Test. 29 (2010) 766–770, https://doi.org/10.1016/J.POLYMERTESTING.2010.04.001.
[60] T.A. Sebaey, N. Blanco, J. Costa, C.S. Lopes, Characterization of crack propagation in mode I delamination of multidirectional CFRP laminates, Compos. Sci. Technol. 72 (2012) 1251–1256, https://doi.org/10.1016/J.COMPSCITECH.2012.04.011.